Strain Path Influence on Formability and Microstructural Evolution of IFHS Steel via Miniature LDH Test

Pavan Kumar[1], *Peeyush* Mahajan[1], *Sushil* K. Mishra[1], *Rahul* Datta[2], and *K.* Narasimhan[1*]

[1]Indian Institute of Technology Bombay, Mumbai, 400076, India
[2]National Institute of Technology, Warangal, 506004, India

Abstract. This work investigates effect of strain path on the forming behaviour and microstructural evolution of Interstitial Free High Strength (IFHS) steel using miniature Limiting Dome Height (LDH) test. Miniature samples representing uniaxial, plane strain, and biaxial conditions were fabricated from 0.7 mm thick IFHS steel sheets and deformed up to necking using the miniature LDH test to generate Forming Limit Diagram (FLD). The microstructural changes occurred along different strain paths were analysed on deformed miniature samples using Electron Backscattered Diffraction (EBSD) and X-ray Diffraction (XRD) techniques. IPF map showed almost similar level of deformation in the neck and near neck region of the plane strain sample. In case of uniaxial and biaxial samples high fraction of non-indexed zone were noted in the neck region compare to the near neck region due to the localized deformation. Texture analysis revealed higher 'BRASS' and 'GOSS' intensities in the neck region of uniaxial specimens, indicating greater deformation. Biaxial specimens at neck and near neck region showed 'RCUBE' rotation to 'CUBE' texture, enhancing isotropy for better formability. In case of plane strain sample textures such as 'COPPER', 'BRASS', and 'S' were notably low, likely due to reduced strain levels in the deformation mode.

Keywords: Forming limit diagram; Miniature LDH test; Microstructure; IFHS steel.

1 Introduction

Forming limit diagrams (FLDs) serve as a crucial tool for evaluating the formability of sheet metals by identifying critical strain states that lead to localized necking or failure. Since their inception by Goodwin in 1968 [1], FLDs have been extensively utilized in sheet metal forming analysis to understand material behaviour under varying loading conditions. Several factors influence FLDs [2], including strain path, sheet thickness, grain size, and crystallographic texture. The Nakajima test has been established as a standard method for determining the forming limits of both thick and thin sheet materials. Researchers [3,4] have conducted extensive studies using this test and have reported that the surface characteristics of the material play a crucial role in its formability. Variations in surface roughness and texture can significantly influence strain localization and fracture initiation during deformation. Furthermore, in case of thin sheets [5,6] , the use of smaller tools can introduce scaling effects, potentially altering the material's deformation behaviour and forming limits due to size-dependent material responses and contact mechanics at the microscale. Size effect [7,8] greatly impact the formability of the thin sheet and limit dome height (LDH) test was used to determine the FLD of the material. In sheet metal forming, particularly with thin sheets, lubrication is essential for enhancing material formability. Effective lubrication reduces friction between the tool and the workpiece, thereby minimizing wear, preventing defects, and improving the overall quality of the formed parts. Different researchers [9,10] investigated the effectiveness of technological lubricants in sheet metal forming and they found that the use of such lubricants significantly reduced the coefficient of friction and prevented the sticking of the formed material to the tool surfaces, thereby enhancing formability. Along with the experimental way of predicting the FLD of material, different models [11–14] such as stress based, strain based, shear based and polar effective plastic strain (PEPS) based has been developed for the accurate way to predict FLD of the different material. Morteza et al. [15] made substantial improvements in predicting the formability of various materials by utilizing the BBC criterion. Additionally, previous studies [2,16,17] have demonstrated that stress-based and PEPS (Prediction of Effective Plastic Strain) approaches can accurately estimate forming limit diagrams (FLDs) when used in conjunction with constitutive models such as Swift, Hollomon, and Voce. Furthermore, it has been observed that through-thickness stress plays a more dominant role in influencing formability compared to shear stress, highlighting its critical impact on deformation behaviour.

Along with the mechanical aspects, microstructure and texture play a significant role in understanding the deformation behaviour of the material particularly at the

* Corresponding author: nara@iitb.ac.in

micro-scale. Very few literatures [18–20] have discussed the FLD for thin sheets in relation to microstructural aspects. Bhargava et al. [21] and Shanta et al. [22] investigated the high strength steel with the consideration of evolution of microstructure and found that the formability in the biaxial strain path decreases due to decrease in the fraction of the gamma fiber. Mishra et al. [23] also investigated the effect of strain and strain path on the texture and the twin formation and found that the twin boundary length is higher in the biaxial strain path compared to the uniaxial strain path. Also, twin formation was there in the brass, copper and the Goss orientation texture which led to higher misorientation development. Similarly, there are different researchers [24,25] also carried out the study of microstructure and texture evolution during the uniaxial tension and it was found that the grain with <101> orientation have the lowest dislocations density which specifically refers to the low density of geometrically necessary dislocations (GNDs).

The present work investigates the effect of strain paths on the forming behaviour and microstructure of IFHS steel using miniature LDH tests. Miniature specimens were deformed up to necking, and microstructural changes were analysed with EBSD and XRD.

2 Material and methods

In the present work the interstitial free high strength (IFHS) steel sheet of 0.7 mm thickness is considered. To obtain the mechanical properties of the material uniaxial tensile test was performed according to ASTM E8 standard with a cross-head speed of 3 mm/min. The stress strain curve is depicted in Fig. 1.

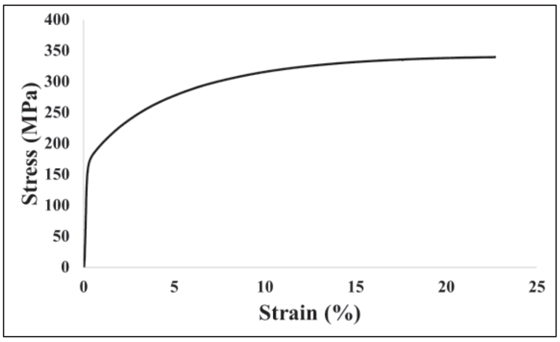

Fig. 1. Stress-strain curve.

Initially the fabrication of miniature samples in three conditions: uniaxial, plane strain and biaxial from the as-received sheet has been done. The dimensions of the miniature samples are shown in Fig. 2.

After fabrication the samples were deformed up to necking through miniature LDH test. The necking zone of the fabricated samples were subjected to the strain measurement and microstructural study. The methodology of this work is summarized in the Fig. 3.

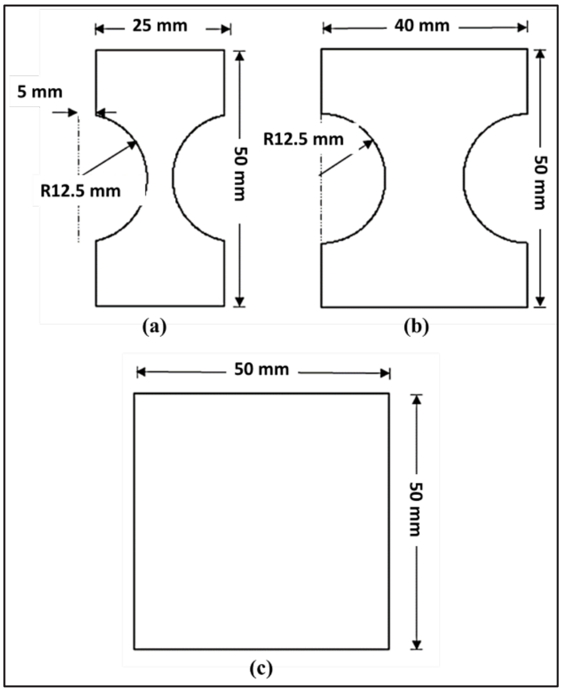

Fig. 2. Dimensions of miniature samples; (a) Uniaxial, (b) Plane strain, and (c) Biaxial

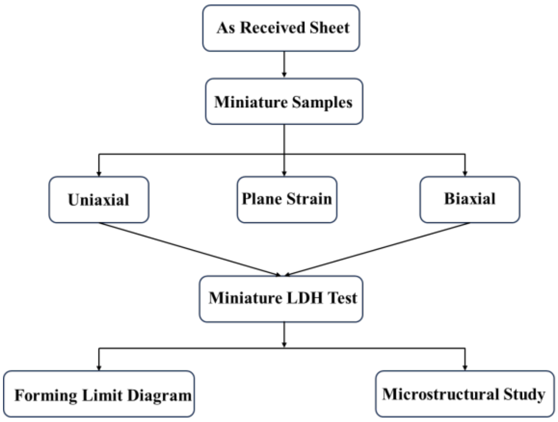

Fig. 3. Methodology of the work

3 Experimentation

As mentioned earlier, this work explores the influence of strain paths on the forming behaviour and microstructural evolution of IFHS steel through miniature LDH tests. The experiments were conducted using a novel, custom-designed setup, illustrated in Fig. 4, integrated with a Tinius Olsen tensile testing machine. A uniform cross-head speed was employed across all strain paths: uniaxial, plane strain, and biaxial. The setup consisted of four key components: a top die, bottom die, C-clamp, and punch. Samples with dot patterns were positioned between the top and bottom dies during testing. To ensure sufficient blank holding force and avoid drawing or wrinkling, four C-clamps with bolts were utilized. Automotive grease was applied as a lubricant at the sheet-punch interface.

Before testing, sample surfaces were electrochemically marked with 1 mm diameter circles, spaced 2 mm apart, forming a dot pattern. Upon deformation, these circles turned into ellipses. The deformed samples were scanned using an Alicona stereo microscope, and images were analysed to determine plastic strain (major and minor strains). The ellipse in the neck region, as shown in Fig. 5 (a), was used to calculate forming limits by measuring the major and minor diameters.

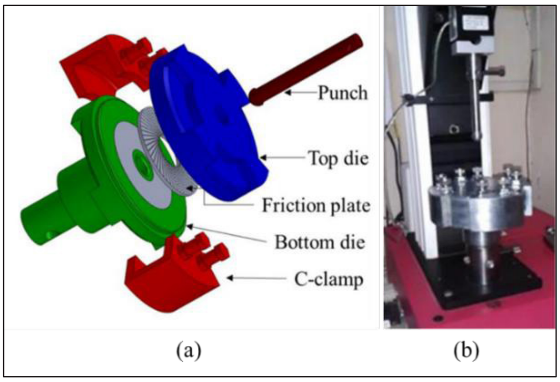

Fig. 4. Miniature LDH setup; (a) CAD model (b) Setup on tensile test machine.

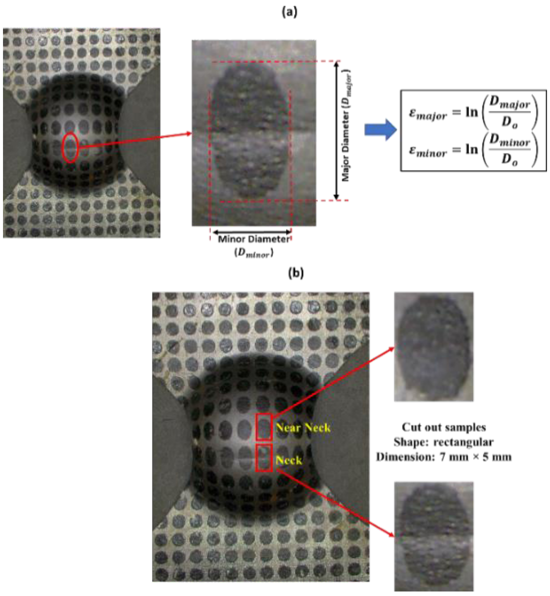

Fig. 5. (a) Experimental strain measurement, and (b) Sample size for microstructural analysis

The following equations were used to measure the minor and major strain on the deformed samples at necking zone.

$$\varepsilon_{minor} = \ln\left(\frac{d_{minor}}{d_o}\right) \quad (1)$$

$$\varepsilon_{major} = \ln\left(\frac{d_{major}}{d_o}\right) \quad (2)$$

EBSD and texture analysis were performed at targeted locations (neck and near-neck zones) of the deformed samples (Fig. 5 (b)). Specimens were prepared by wire EDM cutting, followed by mechanical polishing and electropolishing to achieve the required surface quality. Electropolishing was carried out at 20 volts for 20 seconds using an electrolyte composed of 20% methanol and 20% perchloric acid. The EBSD analysis was conducted using a ZEISS Auriga Compact Crossbeam FIB FEG equipped with an EDAX Velocity detector, at 500X magnification with a 20V acceleration voltage. Scans covered a 300x300 µm area with a 0.5 µm step size. Data processing was done using TSL OIM software, ensuring a confidence index (CI) above 0.1. Grains were identified by continuous boundaries and misorientations greater than 2° {Low Angle Grain Boundary (LAG): 2°–15°, High Angle Grain Boundary (HAG): >15°}. Parameters such as grain size, average misorientation (GAM), kernel average misorientation (KAM), and grain orientation spread (GOS) were measured. A GOS threshold of 2° was used to differentiate deformed grains from recrystallized ones. KAM was calculated using the third-neighbour kernel, excluding misorientations greater than 5°.

4 Results and discussion

This study investigated the influence of strain paths on forming limit diagrams (FLD) using miniature LDH tests. The main findings, encompassing FLD behaviour as well as microstructural and textural changes, are discussed below.

4.1 Forming limit diagram

As previously mentioned, the samples were prepared for three distinct strain paths: uniaxial, plane strain, and biaxial to evaluate the forming limits using the miniature LDH test. Deformation was carried out up to the necking stage, where the ellipse in the necking region was analysed to determine the forming limits and construct the FLD. The resulting FLD is presented in Fig. 6.

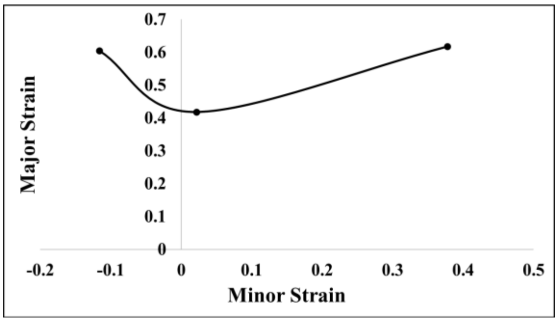

Fig. 6. Forming limit diagram

The plotted FLD demonstrates good stretchability and drawability across all regions. In the biaxial tension region, the material achieves a maximum minor strain of approximately 37% and a maximum major strain of around 61%. Under plane strain region, the limiting major strain is observed to be about 41%. In the uniaxial region, the FLD exhibits a minor strain of 11% and a major strain of 60%. These results are indicating good formability in all regions. However, the forming limit curve (FLC) shows a noticeable asymmetry, being skewed more toward the right side compared to the left side. Narayanasamy et al. [26] deformed the IF steel sheet of 0.6 mm thickness using out of plane stretch-forming experiment. Their results show the similar minor strain equivalent to the corresponding minor strain of the drawing region of the present work (Fig. 6). However, in the present investigation the minor strain was significantly high in the biaxial region compare to the cited work. The higher minor strain in the biaxial region can be attributed to factors such as grain size effects, surface roughness, strain gradient effects, and the fracture behaviour of the specimens, all of which contribute to variations in the results.

4.2 Microstructural studies

The microstructural characteristics formed during different stages of deformation were analysed using EBSD and texture analysis. The investigation focused on the neck and near-neck regions, examining microstructural evolution under various conditions. The results, covering stages from the as-received state to uniaxial, plane strain, and biaxial deformation, are discussed in this section. Fig. 7 displayed the evolution of microstructure parameters (grains size, GOS, KAM and GAM) across different strain path conditions from as-received state to neck and near neck region.

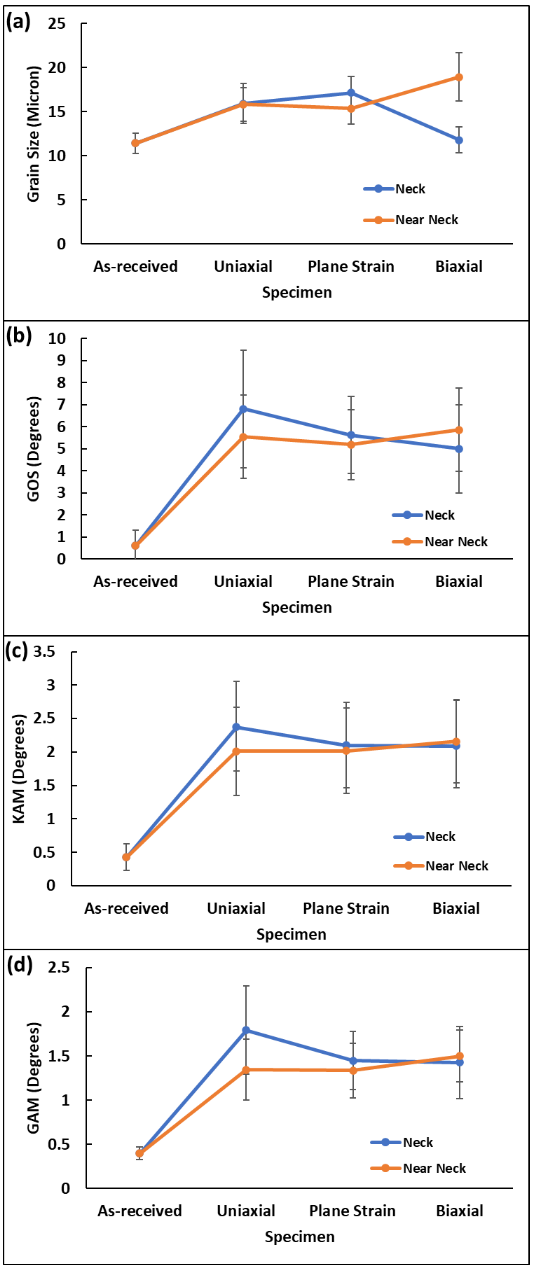

Fig. 7. Variation of microstructure parameters at neck and near neck region; (a) Grain size, (b) GOS, (C) KAM, (d) GAM

Further, Fig. 8 presents the inverse pole figure (IPF) maps and grain boundary misorientation maps of neck and near neck region for different strain path conditions.

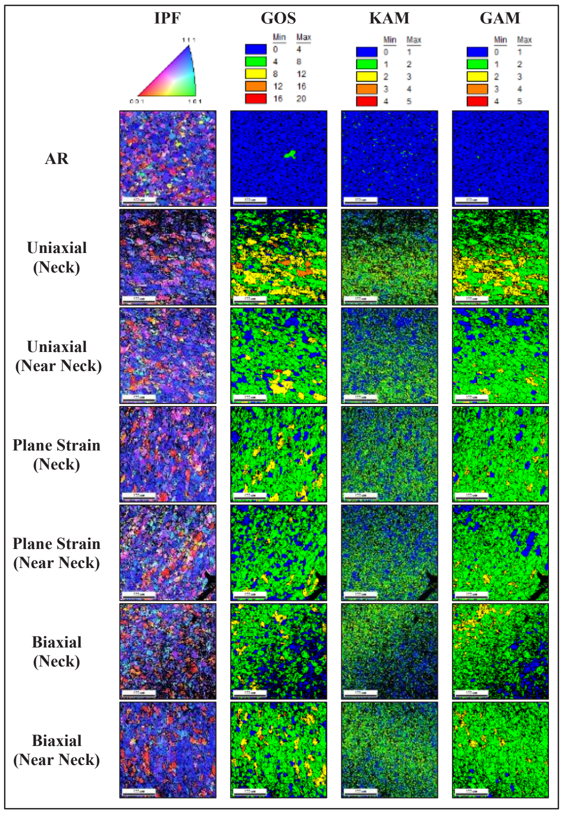

Fig. 8. Inverse pole figures and grain boundary misorientation maps for various strain path conditions

The IPF map of the as-received specimen shows that the grains are mostly equiaxed in nature with the preferable orientation towards <111> which signifies the rolled condition of the sheet. However, due to the thermo-mechanical treatment of the processing route the grains were mostly free from any stored cold work energy or dislocation density which was also reflected from the corresponding GAM, KAM and GOS in Fig. 7. From Fig. 7 (a) it is clear that when the specimens were deformed from as-received state to uniaxial mode of deformation, the average grain size had increased in both neck and near neck region in a similar pattern. However, if the grain distribution from the IPF maps is observed it is visible that the sizes and geometries of the grain are quite different between these two regions. In the neck region, there are more non-indexed and stretched grains, likely due to the higher localized deformation. Despite these differences, the overall average grain size is similar in both the neck and near-neck region.

Sedighiani et al. [27] have reported that with increase in localized deformation or non-uniformity in the strain, the misorientation parameters (GOS, KAM and GAM) tend to increase with the differences in the deformation levels of neck and near neck zone (the deformation in near-neck being much uniform in nature). The similar phenomenon was observed in the plot of average GOS, KAM and GAM (Fig. 7 (b), Fig. 7 (c), Fig. 7 (d)) of the present work. The neck region exhibited significantly higher grain orientation spread

(GOS) and local misorientations (GAM and KAM) compared to the near-neck region. The overall reduction of the average local misorientations in neck region from the uniaxial mode of deformation to plane strain deformation can directly linked to the baseline FLD, i.e. the drop of effective strain in the plane strain region from uniaxial region. However, this reduction of misorientations is almost negligible in near neck region. In case of biaxial deformation, the IPF map showed a significantly larger non-indexed area in the neck region compare to the near-neck region, indicating substantial breaking of grains caused by stretching of the grains rather than drawing. Conversely, in the near-neck region, the grains exhibited proper expansion with maximum lattice rotation towards <111> orientation which reflected the biaxial stretching of the specimen. During biaxial stretching in the LDH test, larger grains fragment into smaller grains due to high strain accumulation. Some fraction of the material undergoes recovery, reducing stored dislocation energy. This is captured by a reduction in average GOS value (indicating local softening) in Fig. 7(b) and is visually evident in the GOS distribution map (Fig. 8), where recovered areas show lower misorientation. The combination of grain refinement, recovery, and deformation heterogeneity dictates the final failure behaviour of the material in the LDH test. Moreover, the level of dislocation densification as well as cold work energy accumulated in the specimen was quite higher in the near-neck region in comparison to the neck region due to the absence of potential recovery.

Standard texture components for FCC and BCC materials were determined at Ø2 = 0°, 45°, and 63°, as outlined in Table 1.

Table 1. Standard texture components

S. No.	Texture Component		Plane and Direction	$\varphi_1, \varphi_2, \varphi_3$
1.		CUBE	{001} <100>	45°, 0°, 45°
2.		RCUBE	{001} <110>	0°, 0°, 45°
3.		GOSS	{110} <100>	90°, 90°, 45°
4.		BRASS	{110} <112>	55°, 90°, 45°
5.		FIBERS		
6.		COPPER	{112} <111>	90°, 35°, 45°
7.		R-GOSS	{110} <110>	0°, 90°, 45°
8.		S	{123} <634>	59°, 37°, 65°

To better understand the evolution of texture, the orientation distribution function (ODF) and the volume fraction of texture components were analysed for all samples using MTEX 5.4.0 in combination with MATLAB software. The ODF analysis of the as-received sample indicated a random texture distribution, as shown in Fig. 9.

The microstructural analysis across all conditions revealed that the grains were primarily characterized by blue (COPPER orientation) and red (CUBE or RCUBE orientation) colours. To examine the effect of these orientations on forming limits, two strategies were adopted. The first involved analysing the orientation distribution function (ODF) and texture intensity under each condition, while the second focused on computing and comparing the volume fractions of different texture components obtained from the ODF.

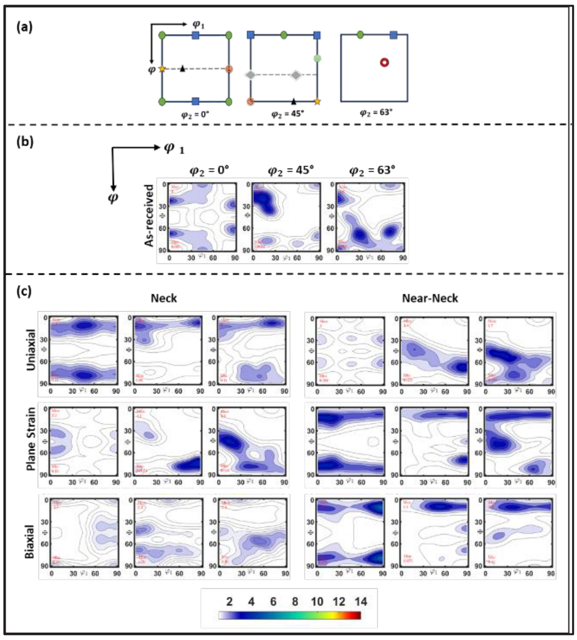

Fig. 9. Orientation distribution function (ODF); (a) Standard texture component (symbol), (b) ODF at as-received state, and (c) Neck and near neck region across different strain path

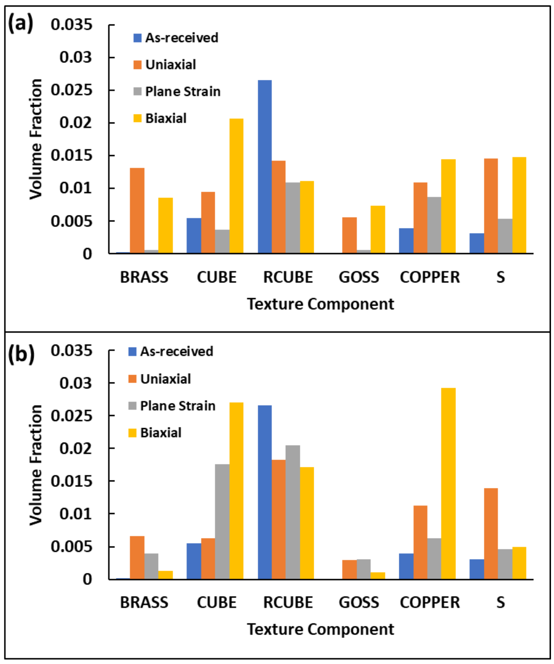

Fig. 10. Volume fraction of texture component; (a) Neck region and (b) Near-neck region

As illustrated in Fig. 10, the as-received sample displayed a significant proportion of RCUBE texture components. Following deformation, the texture distribution became increasingly random. The fraction of RCUBE {001}<110> orientation progressively decreased from the uniaxial to the biaxial deformation condition, while the proportions of CUBE {001}<100>, BRASS {110}<112>, and COPPER {112}<111> orientations increased. A similar pattern was observed in both the neck and near-neck regions, with notable differences in the levels of CUBE {001}<100> and COPPER {112}<111> orientations.

Additionally, the presence of BRASS {110}<112> and GOSS {110}<100> orientations contributed to higher misorientation values. In contrast, the high fractions of RCUBE {001}<110> and COPPER {112}<111> orientations in the AR condition were associated with lower misorientation values. This relationship highlights the impact of texture evolution on the material's deformation behaviour.

5 Conclusions

This research investigated the effect of different strain paths on the forming behaviour and microstructural evolution of IFHS steel using miniature LDH tests. Specimens were deformed up to the necking, and the forming limit diagram (FLD) was developed. Microstructural changes were thoroughly studied using EBSD and XRD techniques. The main conclusions drawn from this study are outlined below.

- The plotted FLD demonstrates excellent stretchability and drawability, with a maximum major strain of 61% in the biaxial region, 41% in the plane strain region, and 60% in the uniaxial region. These results indicate good overall formability,
- The conversion of larger grains to fine grains shows partial recovery, evident in the average GOS value and GOS distribution map of the neck region in the biaxially stretched specimen. Dislocation densification and cold work energy were higher near the neck region due to limited recovery.
- Biaxial specimens showed RCUBE {001} <110> to CUBE {001} <100> rotation at neck and near-neck region, enhancing isotropy and formability. In plane strain samples, COPPER {112} <111> and BRASS {110} <112> textures were low due to reduced strain levels.

References

1. G. M. Goodwin, SAE Technical Papers **380** (1968)
2. D. W. A. Rees, J Mater Process Technol **118**, 1 (2001)
3. N. Ayachi, N. Guermazi, C. H. Pham, and P. Y. Manach, Metals (Basel) **10**, 1 (2020)
4. A. Emanuela and M. Marion, Procedia Eng **183**, 83 (2017)
5. J. Sahu, S. Chakrabarty, R. Raghavan, and S. Mishra, Journal of Strain Analysis for Engineering Design **53**, 517 (2018)
6. C. Sudarsan, K. H. Banker, S. Hazra, R. Bhagat, and S. K. Panda, Advances in Materials and Processing Technologies **5**, 25 (2019)
7. S. Basak, B. S. Katiyar, P. Orozco-Gonzalez, V. H. Baltazar-Hernandez, K. S. Arora, and S. K. Panda, International Journal of Advanced Manufacturing Technology **104**, 1749 (2019)
8. M. Jain, J. Allin, X. Duan, and D. J. Lloyd, Materials Science and Engineering: A **390**, 210 (2005)
9. J. Adamus, W. Więckowski, and P. Lacki, Materials **16**, (2023)
10. M. Ovsik, M. Bednarik, M. Reznicek, and M. Stanek, Lubricants **12**, (2024)
11. T. Chaimongkon, S. Panich, and V. Uthaisangsuk, International Journal of Advanced Manufacturing Technology **115**, 3553 (2021)
12. H. Wang, Z. Wang, Y. Yan, and Y. Xu, Chinese Journal of Mechanical Engineering (English Edition) **36**, (2023)
13. S. Basak and S. K. Panda, International Manufacturing Science and Engineering Conference **49897**, V001T02A063 (2016)
14. A. Wessel, L. Morand, A. Butz, D. Helm, and W. Volk, Int J Mech Sci **275**, (2024)
15. M. Alizad Kamran and B. Mollaei Dariani, Journal of the Brazilian Society of Mechanical Sciences and Engineering **44**, (2022)
16. M. Shakeri, A. Sadough, and B. M. Dariani, Proc Inst Mech Eng B J Eng Manuf **214**, 821 (2000)
17. S. Basak and S. K. Panda, International Manufacturing Science and Engineering Conference **49897**, V001T02A063 (2016)
18. J. Sahu, S. Chakrabarty, R. Raghavan, and S. Mishra, Journal of Strain Analysis for Engineering Design **53**, 517 (2018)
19. K. Rubešová, M. Rund, S. Rzepa, H. Jirková, Š. Jeníček, M. Urbánek, L. Kučerová, and P. Konopík, Metals (Basel) **11**, 1 (2021)
20. T. C. Cheng and R. S. Lee, J Mater Process Technol **253**, 134 (2018)
21. M. Bhargava, S. Chakrabarty, V. K. Barnwal, A. Tewari, and S. K. Mishra, Mater Des **152**, 65 (2018)
22. S. Chakrabarty, M. Bhargava, H. K. Narula, P. Pant, and S. K. Mishra, International Journal of Advanced Manufacturing Technology **106**, 5085 (2020)
23. S. K. Mishra, S. M. Tiwari, A. M. Kumar, and L. G. Hector, Metall Mater Trans A Phys Metall Mater Sci **43**, 1598 (2012)
24. J. Ma, M. Guo, C. Kan, Y. Zhang, L. Xu, Z. Yang, J. Wu, C. Liu, and J. Xu, Mater Today Commun **43**, 111720 (2025)
25. A. A. Saleh, E. V. Pereloma, and A. A. Gazder, Acta Mater **61**, 2671 (2013)
26. R. Narayanasamy and C. S. Narayanan, Mater Des **28**, 1490 (2007)
27. K. Sedighiani, K. Traka, F. Roters, J. Sietsma, D. Raabe, and M. Diehl, Acta Mater **237**, 118167 (2022)